ENERGY RESOURCES

10.1126/sciadv.1501425

Room temperature stable CO_x-free H_2 production from methanol with magnesium oxide nanophotocatalysts

Zhengqing Liu,[1]* Zongyou Yin,[2,3]*† Casandra Cox,[3] Michel Bosman,[4] Xiaofeng Qian,[2] Na Li,[1] Hongyang Zhao,[1] Yaping Du,[1†] Ju Li,[1,2†] Daniel G. Nocera[3†]

Methanol, which contains 12.6 weight percent hydrogen, is a good hydrogen storage medium because it is a liquid at room temperature. However, by releasing the hydrogen, undesirable CO and/or CO_2 byproducts are formed during catalytic fuel reforming. We show that alkaline earth metal oxides, in our case MgO nanocrystals, exhibit stable photocatalytic activity for CO/CO_2-free H_2 production from liquid methanol at room temperature. The performance of MgO nanocrystals toward methanol dehydrogenation increases with time and approaches ~320 μmol g^{-1} $hour^{-1}$ after a 2-day photocatalytic reaction. The CO_x-free H_2 production is attributed to methanol photodecomposition to formaldehyde, photocatalyzed by surface electronic states of unique monodispersed, porous MgO nanocrystals, which were synthesized with a novel facile colloidal chemical strategy. An oxygen plasma treatment allows for the removal of organic surfactants, producing MgO nanocrystals that are well dispersible in methanol.

INTRODUCTION

Because of the high mobility of protons, hydrogen can be efficiently converted into electricity by using low-temperature proton exchange membrane fuel cells. However, it is not easy to store and transport pure hydrogen. A liquid methanol–formaldehyde cycle could be useful for storing hydrogen (*1*)

$$CH_3OH \rightleftharpoons H_2(g) + CH_2O \quad (1)$$

Methanol (CH_3OH) has a boiling point of 64.7°C and is a liquid under ambient conditions. Formaldehyde (CH_2O) has a boiling point of −19.3°C, so only moderate pressure (~5 atm) is needed to liquefy it; furthermore, it exhibits 37 weight percent solubility in liquid water. Reaction (1) in a closed loop releases no carbon into the atmosphere (*2*, *3*). The difficulty in reaction (1) lies in efficient methanol dehydrogenation to produce H_2 at the site of end use (as opposed to hydrogenation, which can be accomplished centrally), and so far, this has been far from economical. The reported dehydrogenation catalysts to producing hydrogen from methanol mainly include aqueous methanol reforming and pure methanol decomposition. Aqueous methanol reforming, with H_2O added for the water-gas (CO) shift reaction, normally requires high temperatures (≥200°C) and pressures (≥25 bar) (*4*, *5*), or mild temperatures (<100°C) but the use of ruthenium complexes (*6*) or lower-stability metal-organic complexes (*7*). For pure methanol decomposition, thermal decomposition is achieved at high temperatures (≥160°C) with noble metals (Pt and Pd) (*8*–*12*), although photodecomposition has been reported at room temperature with Ti-β and noble metals (Pt, Rh, Ir, Pd, and Au) deposited on TiO_2 as photocatalysts. However, the photocatalytic reactions require methanol vapor, and a Pt-TiO_2 catalyst is plagued by low H_2 yields (<7 μmol H_2 g^{-1} $hour^{-1}$) and low stability (*13*–*15*).

Here, we show that magnesium oxide (MgO), a stable and cheap alkaline earth metal oxide that has been used as a photocatalyst for CO_2 reduction and organic contaminant degradation, an additive in refractory materials, and an adsorbent for air purification, toxic waste remediation, and biomedicine (*16*–*25*), is also an ultrastable photocatalyst for hydrogen production from methanol. We can mass produce monodispersed, porous MgO nanoparticles (NPs) with diameters ranging from 40 to 170 nm that demonstrate stable CO_x-free H_2 production from liquid methanol near room temperature.

Various wet chemical synthesis strategies have been developed to obtain MgO nanocrystals. Examples include sol-gel processes, hydrothermal/solvothermal methods, polyol-mediated thermolysis reactions, and microwave-assisted synthesis (*26*–*29*). However, most of the current routes initially yield hydroxide precursors, such as $Mg(OH)_2$ and $Mg_2(OH)_2CO_3$, which must be calcinated at high temperatures to produce crystalline MgO. These high-temperature processes are costly and usually result in fusion of NPs into aggregates (*30*–*33*). To date, only one study focused on the preparation and properties of nearly monodispersed MgO nanocrystals using an organometallic decomposition method (*34*). However, the raw materials used in this approach are toxic and expensive. To the best of our knowledge, until now, a facile, environmentally friendly, and inexpensive synthetic route to mass produce well-defined, porous MgO nanocrystals still remains a challenge, and a systematic study on the synthesis and properties of monodispersed, porous MgO nanocrystals has yet to be performed.

Here, we demonstrate an inexpensive and green approach to synthesizing monodispersed, porous monocrystalline MgO NPs (Scheme 1) using magnesium acetylacetonate dihydrate [$Mg(acac)_2{\cdot}2H_2O$]. The size of the porous MgO nanocrystals can be tuned from ~40 to 170 nm, all showing ultraviolet (UV) to blue emissions under UV light excitation

[1]Frontier Institute of Science and Technology jointly with College of Science, State Key Laboratory for Mechanical Behavior of Materials, Xi'an Jiaotong University, Xi'an 710049, China. [2]Department of Nuclear Science and Engineering, and Materials Science and Engineering, Massachusetts Institute of Technology, Cambridge, MA 02139, USA. [3]Department of Chemistry and Chemical Biology, Harvard University, 12 Oxford Street, Cambridge, MA 02138, USA. [4]Institute of Materials Research and Engineering, A*STAR (Agency for Science, Technology and Research), 2 Fusionopolis Way, Singapore 138634, Singapore.
*These authors contributed equally to this work.
†Corresponding author. Email: ypdu2013@mail.xjtu.edu.cn (Y.D.); zyyin@mit.edu (Z.Y.); liju@mit.edu (J.L.); dnocera@fas.harvard.edu (D.G.N.)

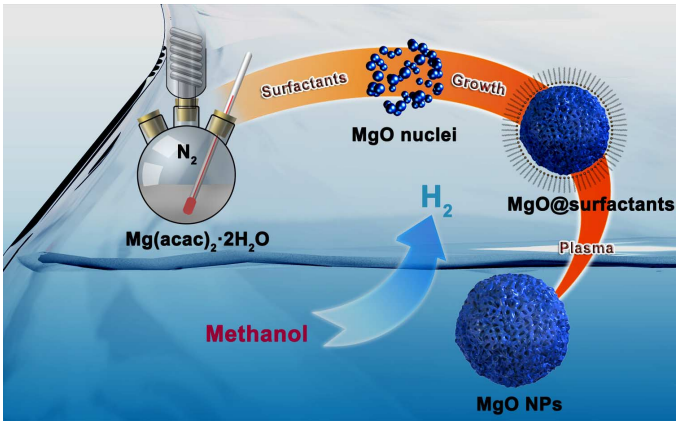

Sheme 1. Process of synthesis of MgO NPs and activity in H_2 production from methanol photodecomposition.

that indicates high density of mid-gap surface electronic states. After oxygen plasma treatment, we modified the surfaces of as-obtained MgO NPs, improving their surface purity and hydrophilicity. The superior activity in CO_x-free H_2 production from MgO NPs was associated with the local photoexcitation and charge separation among MgO defect energy levels, where excited holes oxidize methanol to generate protons that subsequently get reduced by hot electrons to produce H_2.

RESULTS

Synthesis and characterization of monodispersed porous MgO nanocrystals

The synthesized MgO NPs have an exclusively face-centered cubic phase [periclase type, space group: *Fm3m*, JCPDS (Joint Committee on Powder Diffraction Standards): 45-0946], as confirmed by powder x-ray diffraction (XRD) analysis (Fig. 1A) for various-sized MgO NPs, with the calculated crystal parameters $a = b = c = 4.211$ Å. No diffraction peaks from other chemical species, such as $Mg(OH)_2$ or $MgCO_3$, are detectable in all the samples. The average particle sizes of MgO NPs determined by XRD using the Debye-Scherrer equation to the (200) reflection were around 40, 85, 115, and 170 nm, respectively. Sharpening of the diffraction peaks indicates the increased crystallinity of MgO NPs with increasing size.

Figure 1B shows a transmission electron microscopy (TEM) image of as-synthesized MgO nanocrystals; the MgO NPs are relatively monodispersed with an average size of ~85 nm (inset for a histogram of particle diameters). This suggests retention of capping ligands on the nanocrystal surfaces, as validated by Fourier transform infrared (FTIR) spectroscopy (fig. S1). The scanning electron microscopy (SEM; fig. S2A) image shows that the MgO NPs are spherically shaped. Energy-dispersive x-ray (EDX) spectroscopy (fig. S2B) confirms that stoichiometric MgO is formed with an atomic ratio of Mg/O = 1:1.

The size of the MgO NPs was readily controlled by varying the reaction temperature and time. For instance, with 2 mmol of $Mg(acac)_2{\cdot}2H_2O$ as the precursor in oleylamine/oleic acid/1-octadecene (OM/OA/ODE) = 4:1:5 (molar ratio), a reaction time of 30 min at 265°, 280°, 300°, or 320°C produced MgO NPs with an average diameter of ~40 nm (Fig. 1C), ~85 nm (Fig. 1D), ~115 nm (Fig. 1E), or ~170 nm (Fig. 1F), respectively, which is well consistent with the

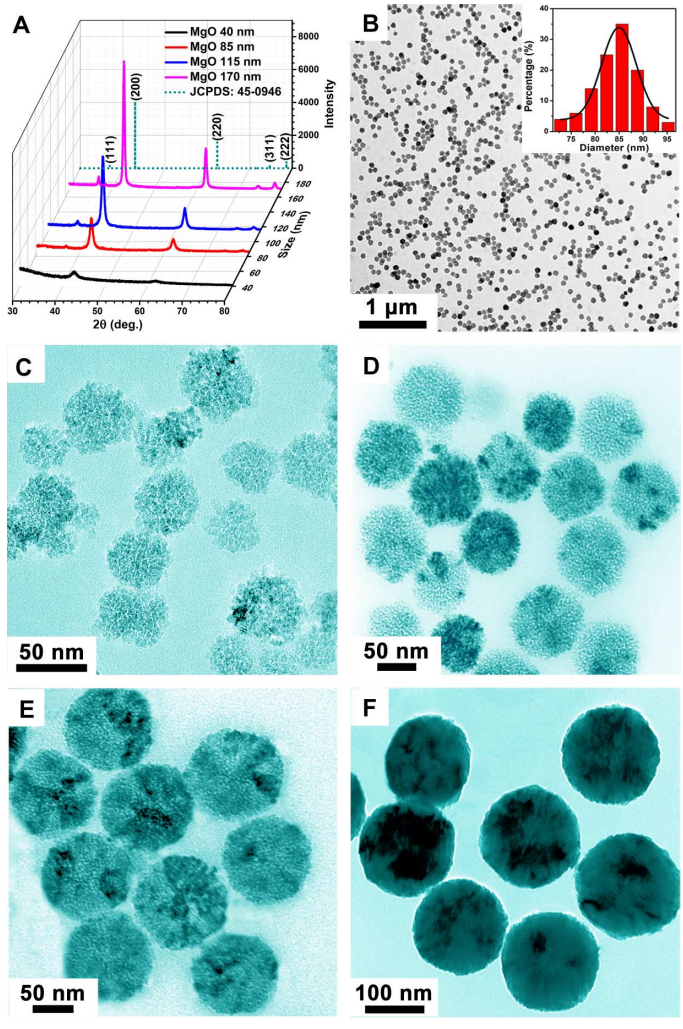

Fig. 1. Composition and morphology characterization of MgO NPs. (**A**) XRD pattern of various-sized MgO NPs. (**B**) TEM image of 85-nm-sized porous MgO NPs, with a plane size distribution analysis (inset). (**C** to **F**) Temperature effect on NP size. TEM images of MgO NPs with different sizes obtained from the thermolysis of 2 mmol of $Mg(acac)_2{\cdot}2H_2O$ in OM/OA/ODE = 4:1:5 (molar ratio) at different temperatures for the same reaction time of 30 min: 265°C (C), 280°C (D), 300°C (E), and 320°C (F). From the TEM images, the average sizes of MgO NPs can be estimated to be ~40 nm (C), ~85 nm (D), ~115 nm (E), and ~170 nm (F), respectively.

XRD analysis (Fig. 1A). Moreover, as indicated by the TEM images in Fig. 1, the as-obtained MgO NPs gradually became smooth as the reaction temperature was elevated. Under a fixed reaction temperature of 265°C, the thermolysis of 2 mmol of $Mg(acac)_2{\cdot}2H_2O$ in OM/OA/ODE = 4:1:5 (molar ratio) for 60 min produces MgO NPs with a size of ~60 nm (fig. S3A). When the reaction temperature was raised to 280°C with all other conditions unchanged, the size of MgO NPs increased to ~100 nm (fig. S3B). Our results show that the size of the as-obtained MgO NPs did not significantly change with the reaction time (30 to 60 min) and when the temperature was kept constant at 300° or 320°C (Fig. 1E versus fig. S3C and Fig. 1F versus fig. S3D). This suggests a temperature-driven "size-focusing" process with increasing reaction temperature (*35*).

The crystal structure of the individual MgO NPs was determined with high-resolution TEM (HRTEM) imaging and selected-area electron diffraction (SAED), as shown in Fig. 2. Figure 2A represents a typical TEM image for a single MgO NP; an amorphous surface layer can be clearly observed at the edge of the MgO NPs (inset of Fig. 2A). This amorphous surface layer may result from the applied capping ligands (OM and OA), which is consistent with the FTIR spectroscopy (fig. S1). The enlarged TEM image in the inset of Fig. 2A and the high-angle annular dark-field scanning TEM (HAADF-STEM) image in Fig. 2B demonstrate the local variation in density due to the porous nature of the MgO NPs. As seen in Fig. 2C, the HRTEM images taken from Fig. 2A show clear rock salt crystal lattice along the [100]. The observed interplanar distances between the lattice fringes are 0.21 and 0.15 nm, corresponding to the (200) and (220) planes of MgO, respectively. The SAED pattern acquired on a single MgO NP displays a single set of clear diffraction spots (Fig. 2D), confirming the monocrystalline nature of the porous MgO NPs (*36*).

In the present synthesis, the combination of different capping ligands was found to play a key role in obtaining monodispersed porous MgO nanocrystals. For example, aggregated MgO NPs (fig. S4A) were produced when 2 mmol of $Mg(acac)_2{\cdot}2H_2O$ was used as a precursor for a reaction at 280°C for 30 min, with the sole use of OM as the capping ligand and ODE as the solvent. In pure OA and ODE, almost no solid matter appeared after the precipitation treatment. In addition, we found that different ratios of solvents had great influence on the dispersibility of the porous MgO nanocrystals (fig. S4, B to D). High yields of monodispersed porous MgO nanocrystals were only obtained at an optimized OM/OA/ODE ratio of 4:1:5 (Fig. 1B) because of a well-maintained balance between nucleation and growth during synthesis.

Through manipulation of capping ligands, solvents, and their relative ratios, we have successfully synthesized size-controlled monodispersed porous MgO NPs. One unique characteristic of MgO is its chemical stability, which is essential for long-term performance under strong illumination. To remove surface capping ligands, we used an oxygen plasma treatment on dried MgO powders. As an example, fig. S1 shows a comparison between the FTIR spectrum of the 85-nm MgO NPs before (black) and after (red) treatment. The oxygen plasma treatment thus efficiently modifies the nanomaterial surface by removing the organic capping ligands.

Figure 3 shows the room temperature UV-vis (visible) absorption and photoluminescence (PL) spectra for MgO NPs. Figure 3A shows the UV-vis absorption spectra for MgO NPs of different sizes. All of the colloidal MgO NPs exhibited continuous absorption across the UV wavelength range, with two broad absorption peaks centered around 220 nm (5.6 eV) and 270 nm (4.6 eV). These peaks arise from the excitation of O^{2-} surface anions on the edge (fourfold coordinated) and on the corner (threefold coordinated) of the nanocrystal (*37*, *38*), respectively. Although MgO is a wide–band gap insulator (E_g = 7.8 eV) (*39*, *40*), optical transitions in the visible range were observed for our porous MgO NPs. Figure 3B shows PL spectra of MgO NPs at an excitation wavelength of 270 nm. The broad spectra covering from 300 to 450 nm indicate the presence of structural defects, such as oxygen vacancies (*41*–*43*), in the insulating MgO. All of the various sizes of the MgO NPs exhibited a strong visible blue emission if under 365-nm UV irradiation (fig. S5).

Stable H_2 production from liquid-methanol photodecomposition near room temperature

The photocatalytic activity for hydrogen production from high-purity liquid methanol at room temperature was examined for the MgO NPs (see Materials and Methods for details). The excitation wavelength dependence was studied by using various long-pass filters. As shown in Fig. 4A, there is no H_2 production when 530- or 380-nm long-pass filters are used. However, full-wavelength illumination (200 to 2500 nm) resulted in the production of H_2. This result is consistent with photoactivity arising from 220- and 270-nm excitation of the MgO nanocrystals (Fig. 3A). Hydrogen production was sensitive to MgO concentration in methanol. Figure 4B shows that suspensions of

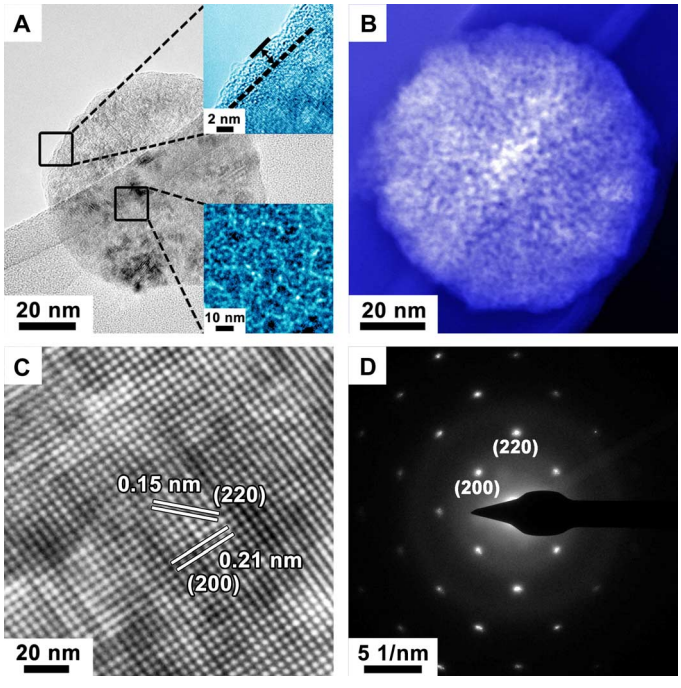

Fig. 2. Crystal structure analysis of MgO NP. (**A** and **B**) TEM (A) and HAADF-STEM (B) image of a single porous MgO NP with a diameter of ~85 nm. Inset of (A): Enlarged TEM images for the edge and center of the MgO NPs. (**C** and **D**) HRTEM image (C) and the corresponding SAED pattern (D) recorded from (A).

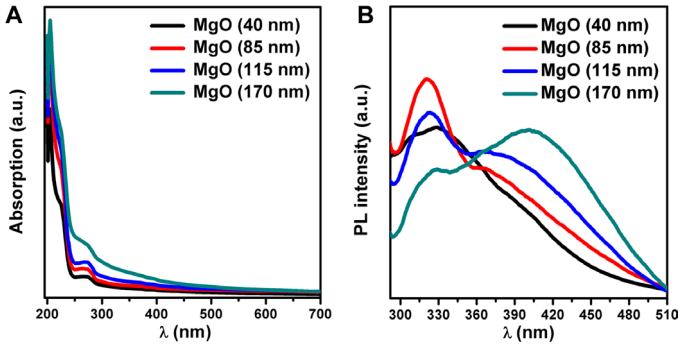

Fig. 3. Optical properties of MgO nanocrystals. (**A** and **B**) Room temperature UV-vis absorption (A) and PL (λ_{ex} = 270 nm) spectra (B) of differently sized porous MgO NPs. a.u., arbitrary units.

~0.38 mg ml^{-1} exhibit the best performance. Lower concentrations likely dilute the concentration of intermediate products, radicals, and/or protons because of the lower availability of surface active sites or photoexcited charges from MgO, resulting in a lower performance. On the other hand, high concentrations can cause light blocking/screening between the adjoining MgO nanocrystals, thus lowering light-harvesting efficiency. This is further supported by the fact that MgO's absorbance of light rises much slower compared with its concentration increase (fig. S6A).

The H_2 production yields for various sizes of MgO nanocrystals are presented in fig. S6. Among the different sizes, the highest H_2 production rates (~55 μmol g^{-1} $hour^{-1}$) occur from 85-nm MgO NPs. The higher surface area of the smaller-sized MgO nanocrystals (85 nm), as compared to the larger-sized MgO nanocrystals (115 and 170 nm), leads to an enhanced photocatalytic reaction with methanol. The surface area was verified using the Brunauer-Emmett-Teller (BET) method: the 40-, 85-, 115-, and 170-nm-sized MgO NPs have surface areas of 28.5, 19.7, 17.4, and 13.9 m^2 g^{-1}, respectively (fig. S7).

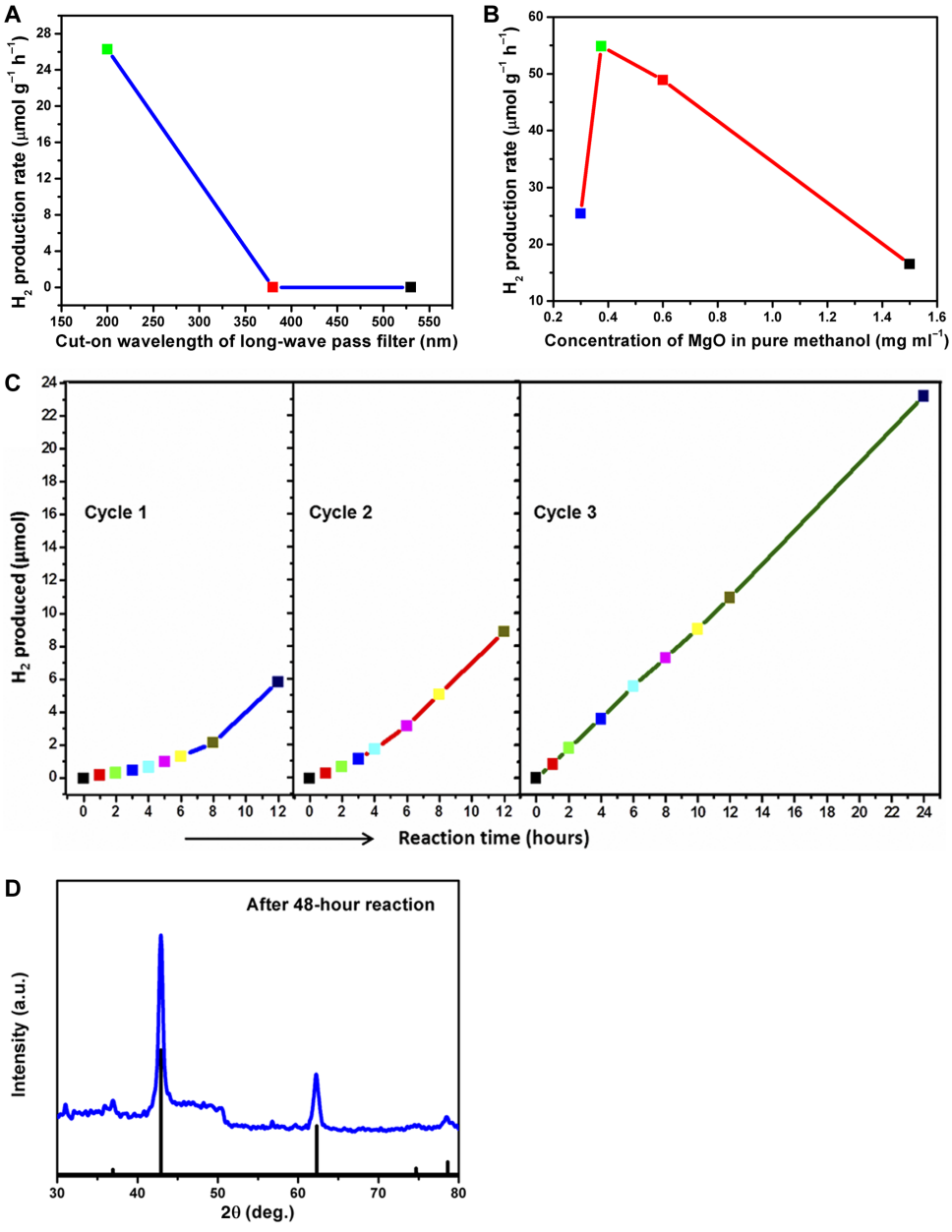

Fig. 4. H_2 production from methanol photodecomposition based on ~85-nm MgO nanocrystals. (**A**) Illumination wavelength effect using the long-wave pass filters with different cut-on wavelengths. (**B**) MgO concentration effect with constant 3 mg of MgO powder dispersed in different volumes of methanol. (**C**) Performance endurance of H_2 production by continuing to use the same MgO (3 mg)/methanol (8 ml) reaction materials for the whole three-cycle testing. (**D**) XRD pattern for MgO after a total 48-hour photocatalytic reaction.

The smallest-sized MgO nanocrystals (40 nm), with the largest BET surface area, did not yield the highest H_2 production rate per weight. This is most likely the result of the lower crystal quality of 40-nm-sized MgO nanocrystals (fig. S8) as compared to the 85-nm-sized MgO nanocrystals (Fig. 2D). The production of H_2 from pure MgO nanocrystals indicates that photoexcited electrons and holes in the surface defect energy levels of MgO can be harvested to oxidize methanol and reduce the generated protons (H^+) for H_2 production. At the same time, this result demonstrates that an oxygen plasma treatment is an effective method to remove the organic surfactants from nanomaterials synthesized via this oil phase strategy. After oxygen plasma treatment, MgO crystals have hydrophilic surfaces and become dispersible in polar liquids, such as methanol and water. This method enhances the direct contact between the MgO nanocrystal surface and methanol, enabling a more efficient photoreaction.

The H_2 production from MgO NPs is stable, and the rate actually improves with time (Fig. 4C and fig. S9). This is in contrast to many H_2 production systems, which often deteriorate in performance over time (*5*, *7*, *15*, *44*, *45*). To test MgO's performance stability, we monitored product analysis of the same MgO/methanol system under photocatalytic reaction over the course of 2 days. To avoid undesirable gas leakage from the capped septum of a reactor during periodic syringe removal of products from the cell, the reaction system was interrupted and then vented in fume hood between testing cycles. During the first cycle, the produced H_2 rises steadily, increasing with time. After the interruption following cycle 1, the production of H_2 continues and its rate increases with time in cycle 2. Hydrogen production continues in cycle 3, although to a lesser extent in rate increase. Notably, the rate reaches ~320 μmol g^{-1} $hour^{-1}$ at the end of a 2-day photocatalytic reaction. The local temperature induced by the lamp illumination around the photoreactor was observed to vary from 25° to 37°C over the 2-day reaction period. Note here that the temperature does not rise with illumination time strictly linearly: the temperature is relatively high, ~37°C, around noon and does not surpass 33°C during other times. The temperature therefore did not affect the performance, and the rising performance during the first 24-hour reaction (Fig. 4C and fig. S9) occurred as the surface sites on MgO NPs were gradually activated while the reaction was ongoing. On the basis of our experimental results, MgO nanocrystals are extremely stable under operating conditions for H_2 production near room temperature. This is attributed not only to the large band gap and high chemical stability of MgO (the heat of formation is 601.24 kJ mol^{-1} of oxygen, in contrast to 469.36 kJ mol^{-1} of oxygen for TiO_2) but also to photocatalytic surface states. To our knowledge, this work is the first to demonstrate catalytic methanol photodecomposition using the surface states of a dielectric oxide nanomaterial synthesized with a low-cost, high-throughput, green process.

Insight into H_2 production from MgO/methanol

Figure 5 proposes a mechanism for the H_2 production of MgO in methanol (*46*, *47*). In this figure, the black dotted lines close to the central solid line represent the broad emission feature of MgO. For comparison, the energy scale versus E_{vac} is scaled to the redox potential versus the normal hydrogen electrode (*46*, *47*). The oxidation potential for methanol, ~−4.3 eV versus E_{vac} at pH 7, is indicated by the dashed pink line. Absolute energy levels for emission and absorption are set on the basis of the fact that MgO NPs have photocatalytic activity in H_2 production. This requires that the oxidation potential of

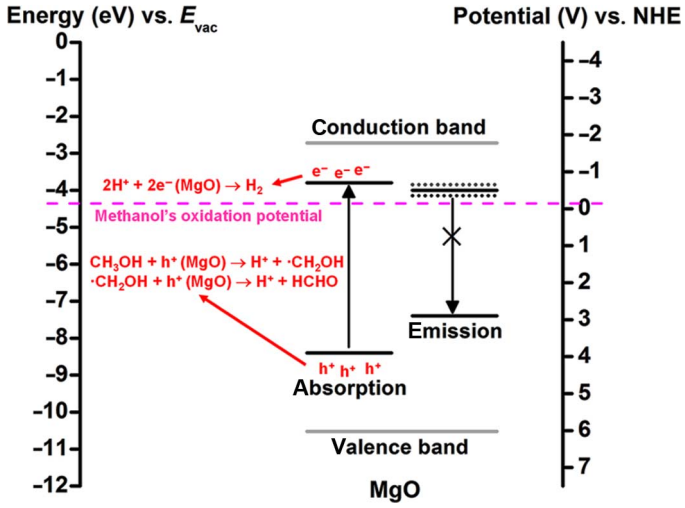

Fig. 5. Schematic diagram of proposed hydrogen production mechanism for MgO nanocrystals. On the basis of the UPS results (fig. S11), the valence band maximum for MgO, that is, E_v, is ~−10.5 eV relative to vacuum. Combined with the 7.8-eV band gap of MgO, we infer a conduction band minimum, E_c, of −2.7 with respect to the vacuum energy level (E_{vac} = 0). The energy levels of the absorption at 4.6 eV arise from surface excitons, as described in the main text. The energy levels of the emission in MgO are derived from the PL spectrum of 85-nm-sized MgO in Fig. 3B, that is, an emission peak at 330 nm with a broad shoulder at around 400 nm. NHE, normal hydrogen electrode.

methanol lies between the energy levels of excitonic electrons and holes in the absorption region of MgO. Surface-bound electron-hole pairs from threefold/low-coordinate surface sites of MgO NPs are ionized after absorption of UV light mainly at 220 nm (5.6 eV) and 270 nm (4.6 eV) (see Fig. 3A) (*37*, *38*, *43*). For simplicity, only the energy levels in the absorption region relating to the 270-nm peak are illustrated in Fig. 5. The energy level of the photogenerated holes of MgO is over −8 eV, negative to the oxidation potential of methanol at ~−4.3 eV versus the vacuum energy level E_{vac} at pH 7 (*48*). This enables photogenerated holes to oxidize CH_3OH and generate intermediate hydroxyalkyl radical, $\cdot CH_2OH$. These dynamically unstable radicals are easily oxidized to formaldehyde (CH_2O) (*3*, *49*). During the two-step oxidation, two protons are generated and reduced to H_2 from the electrons residing in surface states of MgO. This H_2 production behavior is closely correlated with the unique structure of our synthesized MgO nanocrystals. As shown in fig. S10, we compared time-dependent H_2 production between MgO in this work, commercial MgO, commercial SiO_2, and commercial TiO_2 (P25) NPs. The sizes of commercial MgO, SiO_2, and TiO_2 are about 80 to 100 nm, 30 to 60 nm, and 20 to 40 nm, respectively. Before H_2 production, all samples are treated with the same O_2 plasma. With the continuous light illumination time for 24 hours, H_2 produced from commercial SiO_2 is only 0.4 μmol, and that from commercial MgO reaches 1.1 μmol. However, MgO in this work can reach 2.4 μmol, which is 2.2 and 6.0 times of that from commercial MgO and SiO_2, respectively. Compared with SiO_2 and MgO, commercial TiO_2 (P25) produced H_2 more efficiently at first but slowed down after 12-hour reaction and was surpassed by MgO in this work after 16 hours. This indicates an unendurable performance from commercial TiO_2 (P25). The low performance of commercial SiO_2 implies that O_2 plasma

treatment itself does not make a notable contribution to H_2 production in this work; O_2 plasma treatment is mainly used to make MgO nanocrystals hydrophilic. The obviously more H_2 produced from the MgO in this work, as compared with commercial MgO, demonstrates that the unique structure with low-coordinate surface sites of our MgO directly contributes to efficient H_2 production from methanol under photocatalytic reaction.

Aqueous methanol reforming, one of the methanol dehydrogenation reactions, produces carbon dioxide (CO_2) via the water-gas shift reaction. Conversely, complete decomposition of methanol generates carbon monoxide (CO) and H_2 (*5*). In our MgO/methanol reaction system, neither CO_2 (fig. S11, A and C) nor CO (fig. S12, A and B) was observed in the products. On the basis of this observation, the two main products from MgO/methanol after photodecomposition are H_2, as observed from the chromatogram of fig. S11A, and CH_2O. This indicates that methanol, catalyzed by MgO, is not completely photodecomposed. Although this partial decomposition of methanol is not ideal in terms of H_2 production capacity, the CH_2O product is a convenient liquid in a closed loop (under ~5-atm pressure), as opposed to CO_2 or CO gases. Note here that there is a trace of unknown gaseous component (fig. S11A), which is attributed to the impurities in methanol because this component is also produced after illumination of pure methanol (fig. S11B). Additionally, negligible amounts of oxygen are also present because of the manual injection of gas into the gas chromatograph. Furthermore, to check whether methanol itself produces H_2 under UV light illumination (*50*), H_2 production was monitored from 8 ml of methanol in the absence of the MgO photocatalyst. As shown in fig. S5B, the amount of H_2 produced is only ~0.1 μmol after 10-hour reaction, which is only 2.5% of that (~4 μmol) produced from the MgO/methanol (3 mg of MgO dispersed in 8 ml of methanol). The negligible H_2 produced from pure methanol starts to saturate after a 9-hour reaction (fig. S6B), which implies that the hydrogen is probably produced from the impurities in methanol that eventually decomposed to the inactive species. This saturation in H_2 production is in contrast to the increasing H_2 production for MgO/methanol (Fig. 4C and fig. S9). MgO not only exhibited stable performance; its crystal structure was well maintained after the 48-hour photocatalytic reaction. This is confirmed by the XRD taken after 48 hours of operation, which is still well matched to the standard pattern of JCPDS: 45-0946, as shown in Fig. 4D.

DISCUSSION

Here, we demonstrate to have successfully synthesized porous, monocrystalline MgO NPs via a green and cheap thermolysis process with high yields. The diameter of the MgO nanocrystals can be well controlled from 40 to 170 nm, and these nanocrystals exhibit intense defect-induced blue luminescence under UV excitation. To widen the application of MgO synthesized via an oil phase solution process, we successfully used an oxygen plasma treatment to remove the capping ligands and increase hydrophilicity and dispersion in polar liquids, such as methanol and water. The resulting MgO NPs are photocatalysts for liquid-methanol photodecomposition, resulting in fast CO_x-free H_2 production. The ultrastable catalytic activity for CO_x-free H_2 production demonstrated herein points to new paths to develop environmentally friendly and scalable photocatalysts.

MATERIALS AND METHODS

Chemicals

Magnesium 2,4-pentanedionate hydrate [$Mg(acac)_2{\cdot}2H_2O$, >98%, Alfa Aesar], OM (70%, Sigma-Aldrich), OA (90%, Sigma-Aldrich), ODE (>90%, Sigma-Aldrich), ethanol [analytical reagent (AR)], acetone (AR), glycerin (AR), and cyclohexane (AR) were used as received without further purification.

Synthesis of porous MgO NPs

The synthesis of the 85-nm-sized porous MgO NPs was used as an example. A slurry containing 2 mmol (0.445 g) of $Mg(acac)_2{\cdot}2H_2O$, 16 mmol (4.288 g) of OM, 4 mmol (1.128 g) of OA, and 20 mmol (5.05 g) of ODE in a three-necked flask (100 ml) was heated to 140°C to remove water and oxygen, thus forming a homogeneous light yellow solution. The resulting mixture was heated to 280°C under N_2 and kept at that temperature for 30 min. Upon cooling to room temperature, the nanocrystals were precipitated by adding an excess of ethanol and glycerin (volume ratio of 4:1) and separated from the solution by centrifugation (10,000 rpm, 10 min), followed by drying in an oven at 60°C. The glycerin was used to remove impurities, such as NaCl. The as-prepared dried nanocrystals could be dispersed in various nonpolar organic solvents, such as cyclohexane and toluene. The average yield of nanocrystals was around 55%.

Characterization

TEM images were acquired with a Hitachi HT7700 transmission electron microscope operated at 100 kV. HRTEM micrographs and STEM images were obtained with a Philips Tecnai F20 FEG (field emission gun)–TEM operated at 200 kV. SEM images were characterized through a Quanta F250. Samples for TEM analysis were prepared by drying a drop of cyclohexane solution containing the nanocrystals on the surface of a carbon-coated copper grid. The XRD patterns were obtained using Rigaku D/MAX-RB with monochromatized Cu Kα radiation (λ = 1.5418 Å) and 2θ ranging from 20° to 80°C. Infrared spectra were recorded on a Nicolet 6700 FT-IR spectrometer. UV-vis absorption spectra were measured on a PerkinElmer Lambda 35 UV-vis spectrophotometer. PL spectra were recorded on a Hitachi F-4600 spectrofluorophotometer at room temperature. Nitrogen adsorption-desorption isotherms were measured on a Micromeritics TriStar 3000 porosimeter (mesoporous characterization) and Micromeritics ASAP 2020 (microporous characterization) at 77 K. All MgO NPs samples were outgassed at 160°C for 6 hours under vacuum before measurements. The specific surface areas were calculated on the basis of the BET method. Ultraviolet photoelectron spectroscopy (UPS) measurements were carried out with a Shimadzu/Kratos AXIS Ultra DLD spectrometer, using the HeI radiation (21.21 eV) from a He discharge lamp. Peaks were recorded with a constant energy of 5 eV and a step size of 0.05 eV. The pressure in the analysis chamber was maintained at 4.3×10^{-9} torr.

Measurement of H_2 production

Here, four kinds of materials/powders were tested for the photocatalytic hydrogen production, including MgO nanocrystals with sizes of 40, 85, 115, and 170 nm. Note here that, before the photocatalytic experiments, all the MgO powders were treated with the same oxygen plasma for 1 hour to generate hydrophilic surfaces by removing the hydrophobic organic ligands. The photocatalytic hydrogen production experiments were performed in a ~16-ml quartz flask under

atmospheric pressure at room temperature. For hydrogen production testing, 3 mg of MgO powder was dispersed in pure methanol (anhydrous, 99.8% from Sigma-Aldrich) with its volume varied from 2 to 10 ml, followed by sonication for ~45 min. Then, the quartz flask was sealed with silicone rubber septum, and then the reaction suspension in the flask was degassed with pure nitrogen gas for ~30 min to remove the air inside, keeping the reaction suspension in an inert environment. After degassing, the quartz flask with reaction suspension was transferred and placed before the light source. A 1000-W mercury lamp (MAX-1000, Newport Corporation) was used as a broadband light source covering the wavelength band between 200 and 2500 nm, to trigger the photocatalytic reaction. The light illumination intensity on the flask was ca. 388 mW cm^{-2}. The hydrogen was analyzed by gas chromatography (Agilent 7890A) with the installed gas valve system. During multiple-cycle performance endurance testing, the reaction material MgO/methanol in the reactor was sonicated for ~30 min, and then the whole reaction system was sealed for the subsequent ~30-min degassing to drive away air before the H_2 production testing.

SUPPLEMENTARY MATERIALS

Supplementary material for this article is available at http://advances.sciencemag.org/cgi/content/full/2/9/e1501425/DC1

fig. S1. FTIR analysis of synthesized and oxygen plasma–treated MgO NPs.
fig. S2. SEM image and EDX analysis of synthesized MgO NPs.
fig. S3. Temperature-dependent experiments of synthesized MgO NPs.
fig. S4. Solvent composition–dependent experiments of synthesized MgO NPs.
fig. S5. Digital photographs of different-sized MgO colloidal solution.
fig. S6. Optical properties for ~85-nm MgO nanocrystals and H_2 production from methanol photodecomposition.
fig. S7. Specific surface area of four different-sized MgO NPs.
fig. S8. TEM and SAED images of an MgO NP with a size of 40 nm.
fig. S9. The rate pattern of H_2 production for ~85-nm MgO nanocrystals.
fig. S10. SEM analysis and H_2 production of commercial MgO, SiO_2, and TiO_2 (P25).
fig. S11. Chromatogram analysis of a mixture of gases.
fig. S12. Chromatogram analysis of a mixture of gases.
fig. S13. UPS spectrum for ~85-nm-sized MgO NPs.

REFERENCES AND NOTES

1. G. A. Olah, A. Goeppert, G. K. Surya Prakash, *Beyond Oil and Gas: The Methanol Economy* (Wiley-VCH, Weinheim, ed. 2, 2009).
2. K.-i. Aika, H. Sekiya, A. Ozaki, Selectivities of group VIII metals for the hydrogenation of formaldehyde and the effect of support and promoter. *Chem. Lett.* **12**, 301–304 (1983).
3. R. Hirschl, A. Eichler, J. Hafner, Hydrogenation of ethylene and formaldehyde on Pt (111) and $Pt_{80}Fe_{20}$ (111): A density-functional study. *J. Catal.* **226**, 273–282 (2004).
4. J. W. Shabaker, R. R. Davda, G. W. Huber, R. D. Cortright, J. A. Dumesic, Aqueous phase reforming of methanol and ethylene glycol over alumina-supported platinum catalysts. *J. Catal.* **215**, 344–352 (2003).
5. D. R. Palo, R. A. Dagle, J. D. Holladay, Methanol steam reforming for hydrogen production. *Chem. Rev.* **107**, 3992–4021 (2007).
6. M. Nielsen, E. Alberico, W. Baumann, H.-J. Drexler, H. Junge, S. Gladiali, M. Beller, Low-temperature aqueous-phase methanol dehydrogenation to hydrogen and carbon dioxide. *Nature* **495**, 85–89 (2013).
7. E. Alberico, P. Sponholz, C. Cordes, M. Nielsen, H.-J. Drexler, W. Baumann, H. Junge, M. Beller, Selective hydrogen production from methanol with a defined iron pincer catalyst under mild conditions. *Angew. Chem. Int. Ed.* **52**, 14162–14166 (2013).
8. Y. Matsumura, M. Okumura, Y. Usami, K. Kagawa, H. Yamashita, M. Anpo, M. Haruta, Low-temperature decomposition of methanol to carbon monoxide and hydrogen with low activation energy over Pd/ZrO_2 catalyst. *Catal. Lett.* **44**, 189–191 (1997).
9. Y. Matsumura, K. Tanaka, N. Tode, T. Yazawa, M. Haruta, Catalytic methanol decomposition to carbon monoxide and hydrogen over nickel supported on silica. *J. Mol. Catal. A Chem.* **152**, 157–165 (2000).
10. W. J. Shen, Y. Matsumura, Low-temperature methanol decomposition to carbon monoxide and hydrogen catalysed over cationic palladium species in Pd/CeO_2. *Phys. Chem. Chem. Phys.* **2**, 1519–1522 (2000).
11. J. C. Brown, E. Gulari, Hydrogen production from methanol decomposition over Pt/Al_2O_3 and ceria promoted Pt/Al_2O_3 catalysts. *Catal. Commun.* **5**, 431–436 (2004).
12. W. Cui, L. Feng, C. Xu, S. Lü, F. Qiu, Hydrogen production by photocatalytic decomposition of methanol gas on Pt/TiO_2 nano-film. *Catal. Commun.* **5**, 533–536 (2004).
13. W. Cui, C. Xu, S. Zhang, L. Feng, S. Lü, F. Qiu, Hydrogen evolution by photocatalysis of methanol vapor over Ti-beta. *J. Photochem. Photobiol. A* **175**, 89–93 (2005).
14. G. Halasi, G. Schubert, F. Solymosi, Comparative study on the photocatalytic decomposition of methanol on TiO_2 modified by N and promoted by metals. *J. Catal.* **294**, 199–206 (2012).
15. A. Gazsi, G. Schubert, T. Bánsági, F. Solymosi, Photocatalytic decomposition of methanol and ethanol on Au supported by pure or N-doped TiO_2. *J. Photochem. Photobiol. A* **271**, 45–55 (2013).
16. C.-J. Jia, Y. Liu, H. Bongard, F. Schüth, Very low temperature CO oxidation over colloidally deposited gold nanoparticles on $Mg(OH)_2$ and MgO. *J. Am. Chem. Soc.* **132**, 1520–1522 (2010).
17. K. Teramura, T. Tanaka, H. Ishikawa, Y. Kohno, T. Funabiki, Photocatalytic reduction of CO_2 to CO in the presence of H_2 or CH_4 as a reductant over MgO. *J. Phys. Chem. B* **108**, 346–354 (2004).
18. S. Demirci, B. Öztürk, S. Yildirim, F. Bakal, M. Erol, O. Sancakoğlu, R. Yigit, E. Celik, T. Batar, Synthesis and comparison of the photocatalytic activities of flame spray pyrolysis and sol–gel derived magnesium oxide nano-scale particles. *Mater. Sci. Semicond. Process.* **34**, 154–161 (2015).
19. K. Mageshwari, S. S. Mali, R. Sathyamoorthy, P. S. Patil, Template-free synthesis of MgO nanoparticles for effective photocatalytic applications. *Powder Technol.* **249**, 456–462 (2013).
20. J. I. Di Cosimo, V. K. Díez, C. Ferretti, C. R. Apesteguía, Basic catalysis on MgO: Generation, characterization and catalytic properties of active sites. *Catalysis* **26**, 1–28 (2014).
21. H. Niu, Q. Yang, K. Tang, Y. Xie, Large-scale synthesis of single-crystalline MgO with bone-like nanostructures. *J. Nanopart. Res.* **8**, 881–888 (2006).
22. A. Khaleel, P. N. Kapoor, K. J. Klabunde, Nanocrystalline metal oxides as new adsorbents for air purification. *Nanostruct. Mater.* **11**, 459–468 (1999).
23. R. Richards, W. Li, S. Decker, C. Davidson, O. Koper, V. Zaikovski, A. Volodin, T. Rieker, K. J. Klabunde, Consolidation of metal oxide nanocrystals. Reactive pellets with controllable pore structure that represent a new family of porous, inorganic materials. *J. Am. Chem. Soc.* **122**, 4921–4925 (2000).
24. C. Feldmann, S. Matschulo, S. Ahlert, Polyol-mediated synthesis of nanoscale $Mg(OH)_2$ and MgO. *J. Mater. Sci.* **42**, 7076–7080 (2007).
25. L. Huang, D.-Q. Li, Y.-J. Lin, M. Wei, D. G. Evans, X. Duan, Controllable preparation of Nano-MgO and investigation of its bactericidal properties. *J. Inorg. Biochem.* **99**, 986–993 (2005).
26. S. Utamapanya, K. J. Klabunde, J. R. Schlup, Nanoscale metal oxide particles/clusters as chemical reagents. Synthesis and properties of ultrahigh surface area magnesium hydroxide and magnesium oxide. *Chem. Mater.* **3**, 175–181 (1991).
27. Y. Ding, G. Zhang, H. Wu, B. Hai, L. Wang, Y. Qian, Nanoscale magnesium hydroxide and magnesium oxide powders: Control over size, shape, and structure via hydrothermal synthesis. *Chem. Mater.* **13**, 435–440 (2001).
28. A. Subramania, G. V. Kumar, A. R. Sathiya Priya, T. Vasudevan, Polyol-mediated thermolysis process for the synthesis of MgO nanoparticles and nanowires. *Nanotechnology* **18**, 225601 (2007).
29. S. Makhluf, R. Dror, Y. Nitzan, Y. Abramovich, R. Jelinek, A. Gedanken, Microwave-assisted synthesis of nanocrystalline MgO and its use as a bacteriocide. *Adv. Funct. Mater.* **15**, 1708–1715 (2005).
30. K. Zhu, J. Hu, C. Kübel, R. Richards, Efficient preparation and catalytic activity of MgO (111) nanosheets. *Angew. Chem. Int. Ed.* **118**, 7435–7439 (2006).
31. O. B. Koper, I. Lagadic, A. Volodin, K. J. Klabunde, Alkaline-earth oxide nanoparticles obtained by aerogel methods. Characterization and rational for unexpectedly high surface chemical reactivities. *Chem. Mater.* **9**, 2468–2480 (1997).
32. P. P. Fedorov, E. A. Tkachenko, S. V. Kuznetsov, V. V. Voronov, S. V. Lavrishchev, Preparation of MgO nanoparticles. *Inorg. Mater.* **43**, 502–504 (2007).
33. C. Yan, D. Xue, Novel self-assembled MgO nanosheet and its precursors. *J. Phys. Chem. B* **109**, 12358–12361 (2005).
34. H. R. Moon, J. J. Urban, D. J. Milliron, Size-controlled synthesis and optical properties of monodisperse colloidal magnesium oxide nanocrystals. *Angew. Chem. Int. Ed.* **48**, 6278–6281 (2009).
35. X. Peng, J. Wickham, A. P. Alivisatos, Kinetics of II-VI and III-V colloidal semiconductor nanocrystal growth: "Focusing" of size distributions. *J. Am. Chem. Soc.* **120**, 5343–5344 (1998).
36. F. Wang, C. Li, L.-D. Sun, C.-H. Xu, J. Wang, J. C. Yu, C.-H. Yan, Porous single-crystalline palladium nanoparticles with high catalytic activities. *Angew. Chem. Int. Ed.* **51**, 4872–4876 (2012).

37. S. Stankic, M. Sterrer, P. Hofmann, J. Bernardi, O. Diwald, E. Knözinger, Novel optical surface properties of Ca^{2+}-doped MgO nanocrystals. *Nano Lett.* **5**, 1889–1893 (2005).
38. M. Sterrer, T. Berger, O. Diwald, E. Knözinger, Energy transfer on the MgO surface, monitored by UV-induced H_2 chemisorption. *J. Am. Chem. Soc.* **125**, 195–199 (2003).
39. R. C. Whited, W. C. Walker, Exciton spectra of CaO and MgO. *Phys. Rev. Lett.* **22**, 1428–1430 (1969).
40. M. Klaua, D. Ullmann, J. Barthel, W. Wulfhekel, J. Kirschner, R. Urban, T. L. Monchesky, A. Enders, J. F. Cochran, B. Heinrich, Growth, structure, electronic, and magnetic properties of MgO/Fe (001) bilayers and Fe/MgO/Fe (001) trilayers. *Phys. Rev. B* **64**, 134411 (2001).
41. G. H. Rosenblatt, M. W. Rowe, G. P. Williams Jr., R. T. Williams, Y. Chen, Luminescence of *F* and F^+ centers in magnesium oxide. *Phys. Rev. B* **39**, 10309–10318 (1989).
42. E. Feldbach, R. Jaaniso, M. Kodu, V. P. Denks, A. Kasikov, P. Liblik, A. Maaroos, H. Mändar, M. Kirm, Luminescence characterization of ultrathin MgO films of high crystallinity prepared by pulsed laser deposition. *J. Mater. Sci. Mater. Electron.* **20** (Suppl. 1), 321–325 (2009).
43. P. Rinke, A. Schleife, E. Kioupakis, A. Janotti, C. Rödl, F. Bechstedt, M. Scheffler, C. G. Van de Walle, First-principles optical spectra for *F* centers in MgO. *Phys. Rev. Lett.* **108**, 126404 (2012).
44. C. G. Silva, R. Juárez, T. Marino, R. Molinari, H. García, Influence of excitation wavelength (UV or Visible light) on the photocatalytic activity of titania containing gold nanoparticles for the generation of hydrogen or oxygen form water. *J. Am. Chem. Soc.* **133**, 595–602 (2011).
45. Y. Hou, A. B. Laursen, J. Zhang, G. Zhang, Y. Zhu, X. Wang, S. Dahl, I. Chorkendorff, Layered nanojunctions for hydrogen-evolution catalysis, *Angew. Chem. Int. Ed.* **52**, 3621–3625 (2013).
46. C. G. Zoski, *Handbook of Electrochemistry* (Elsevier, Amsterdam, 2007).
47. S. Linic, P. Christopher, D. B. Ingram, Plasmonic-metal nanostructures for efficient conversion of solar to chemical energy. *Nat. Mater.* **10**, 911–921 (2011).
48. M. J. Berr, P. Wagner, S. Fischbach, A. Vaneski, J. Schneider, A. S. Susha, A. L. Rogach, F. Jäckel, J. Feldmann, Hole scavenger redox potentials determine quantum efficiency and stability of Pt-decorated CdS nanorods for photocatalytic hydrogen generation. *Appl. Phys. Lett.* **100**, 223903 (2012).
49. A. A. Ismail, L. Robben, D. W. Bahnemann, Study of the efficiency of UV and visible-light photocatalytic oxidation of methanol on mesoporous RuO_2–TiO_2 nanocomposites. *Chemphyschem* **12**, 982–991 (2011).
50. K. I. Öberg, R. T. Garrod, E. F. van Dishoeck, H. Linnartz, Formation rates of complex organics in UV irradiated CH_3OH-rich ices. *Astron. Astrophys.* **504**, 891–913 (2009).

Acknowledgments

Funding: We gratefully acknowledge financial support from NSF DMR-1120901 (Massachusetts Institute of Technology), the start-up funding from Xi'an Jiaotong University, 973 Program of China (2012CB619402), the National Natural Science Foundation of China (grant no. 21371140), and China National Funds for Excellent Young Scientists (grant no. 21522106). D.G.N. acknowledges support from the U.S. Department of Energy, Office of Basic Energy Sciences (DE-SC0009565). **Author contributions:** Y.D., Z.Y., D.G.N., and J.L. proposed the whole research direction and guided the project. Y.D. and Z.L. designed and performed the series of synthesis and characterization experiments. Z.Y. and C.C. preformed the H_2 production test. All authors analyzed the experimental results and drafted the manuscript. **Competing interests:** The authors declare that they have no competing interests. **Data and materials availability:** All data needed to evaluate the conclusions in the paper are present in the paper and/or the Supplementary Materials. Additional data related to this paper may be requested from the authors.

Submitted 11 October 2015
Accepted 2 August 2016
Published 2 September 2016
10.1126/sciadv.1501425

Citation: Z. Liu, Z. Yin, C. Cox, M. Bosman, X. Qian, N. Li, H. Zhao, Y. Du, J. Li, D. G. Nocera, Room temperature stable CO_x-free H_2 production from methanol with magnesium oxide nanophotocatalysts. *Sci. Adv.* **2**, e1501425 (2016).

Science Advances

AAAS

advances.sciencemag.org/cgi/content/full/2/9/e1501425/DC1

Supplementary Materials for

Room temperature stable CO_x-free H_2 production from methanol with magnesium oxide nanophotocatalysts

Zhengqing Liu, Zongyou Yin, Casandra Cox, Michel Bosman, Xiaofeng Qian, Na Li, Hongyang Zhao, Yaping Du, Ju Li, Daniel G. Nocera

Published 2 September 2016, *Sci. Adv.* **2**, e1501425 (2016)
DOI: 10.1126/sciadv.1501425

This PDF file includes:

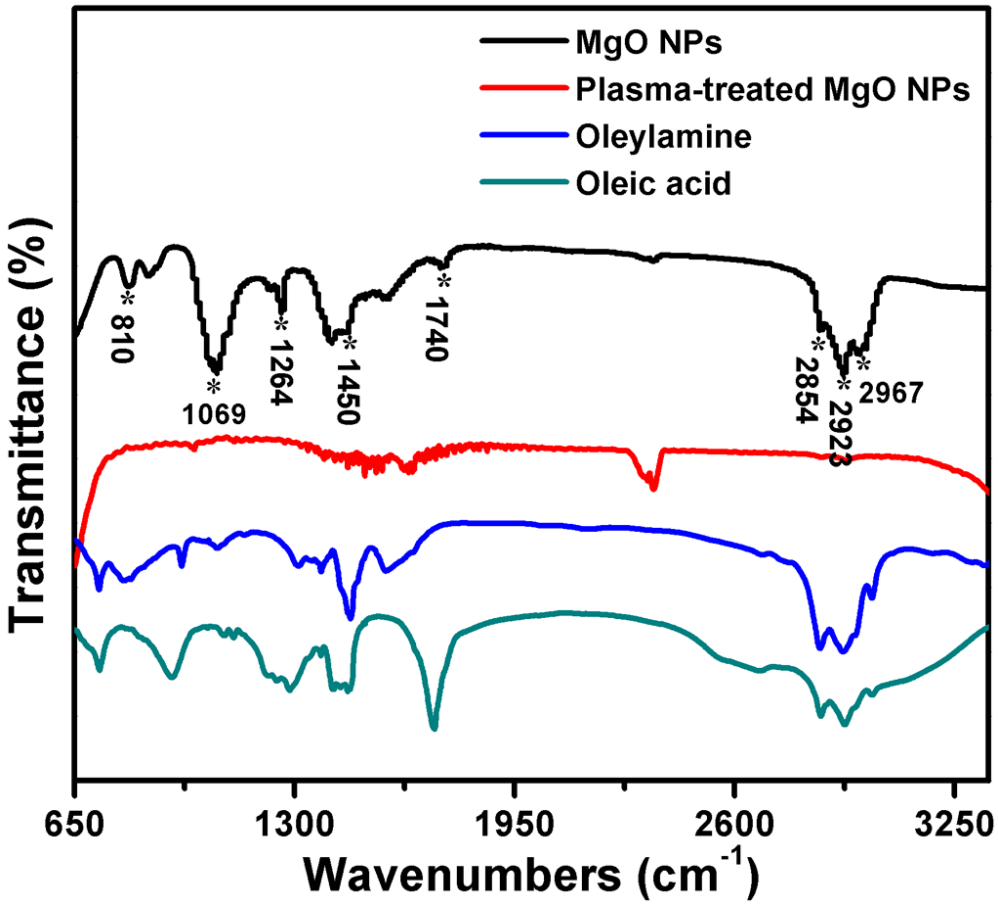

fig. S1. FTIR analysis of synthesized and oxygen plasma–treated MgO NPs. FTIR spectra (Nicolet 6700) of oleylamine, oleic acid, as-prepared MgO NPs and plasma-treated MgO NPs. The presence of acyclic C-H stretching at 2967 cm^{-1}, 2923 cm^{-1} and 2854 cm^{-1} indicate the co-existence of oleic acid and oleylamine. The peaks at 1740 cm^{-1} and 1450 cm^{-1} are assigned to C=O stretch and carboxylate (COO^{-}) stretch, implying the COO^{-} ligand exists on the nanocrystals surface. Additionally, the three sharp peaks at 1264, 1069 and 810 cm^{-1} in the IR spectrum of MgO NPs were indexed to C–N stretch of oleylamine, respectively. Based on the FTIR analysis of MgO NPs, it is confirmed that these MgO nanocrystals are coated by two kinds of organic molecule, oleylamine and oleic acid. Note here, after oxygen plasma treatment, the intensity of characteristic peaks of oleic acid and oleylamine obviously decreased, indicating a successful removal of organic capping ligands from the surface of MgO NPs.

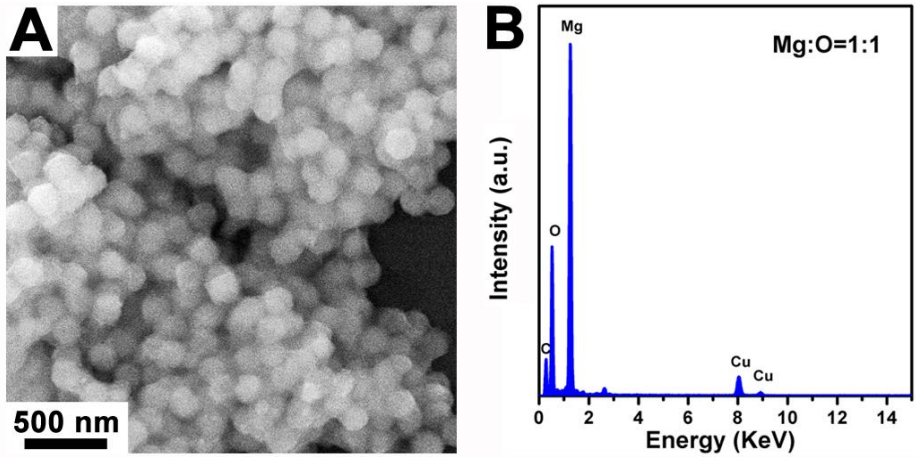

fig. S2. SEM image and EDX analysis of synthesized MgO NPs. (**A**) Scanning electron microscope (SEM) image and (**B**) energy-dispersive X-ray analysis (EDX) spectrum of MgO NPs with size of ~170 nm.

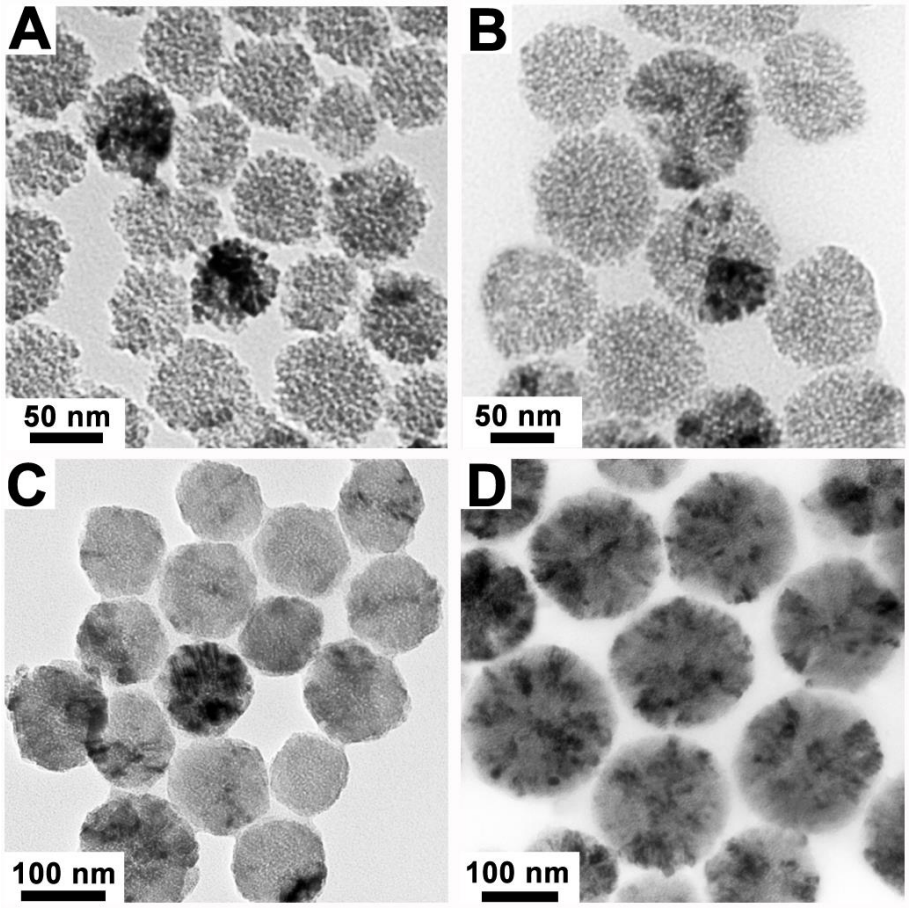

fig. S3. Temperature-dependent experiments of synthesized MgO NPs. TEM images of MgO NPs obtained from the thermolysis of 2 mmol $Mg(acac)_2 \cdot 2H_2O$ in OM/OA/ODE (4:1:5) at different temperature for same reaction time of 60 min. (**A**) 265°C, (**B**) 280°C, (**C**) 300°C, and (**D**) 320°C. From the TEM images, the average sizes of MgO NPs can be estimated to be (**A**) ~60 nm, (**B**) ~100 nm, (**C**) ~115 nm, and (**D**) ~170 nm, respectively.

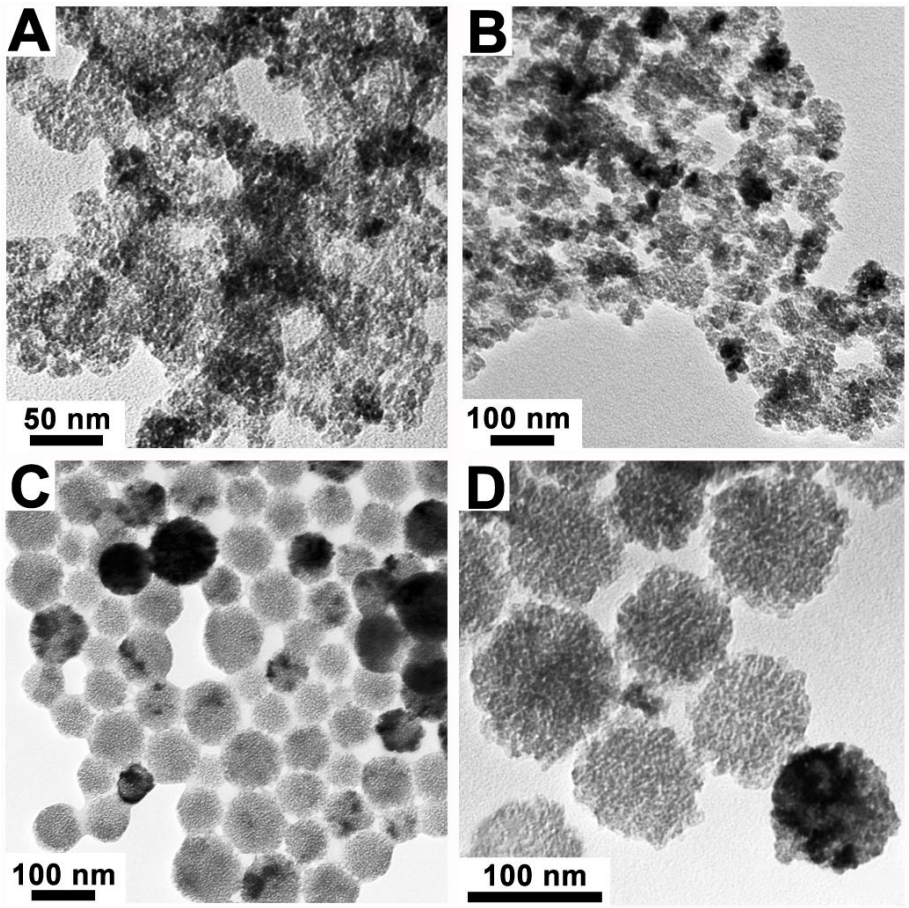

fig. S4. Solvent composition–dependent experiments of synthesized MgO NPs. TEM images of MgO NPs obtained from the thermolysis of 2 mmol of $Mg(acac)_2 \cdot 2H_2O$ in different mixed solvents at 280 °C for 30 min: (**A**) OM:ODE=1:1, (**B**) OM:OA:ODE=14:1:15, (**C**) OM:OA:ODE=8:1:9, and (**D**) OM:OA:ODE=2:1:3.

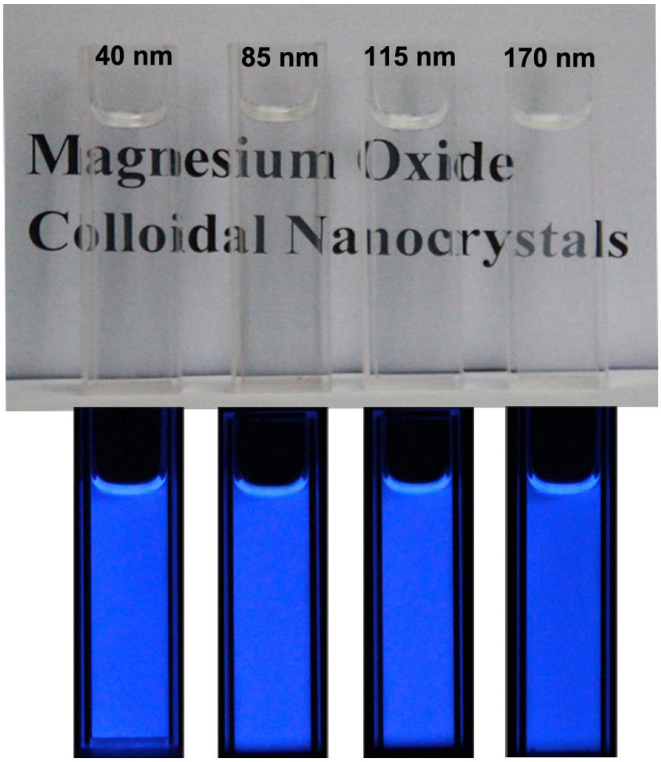

fig. S5. Digital photographs of different-sized MgO colloidal solution.
Photographs of 1 mg mL^{-1} porous MgO NPs dispersed in cyclohexane under ambient illumination (top) and under an irradiation of 365 nm UV light (bottom).

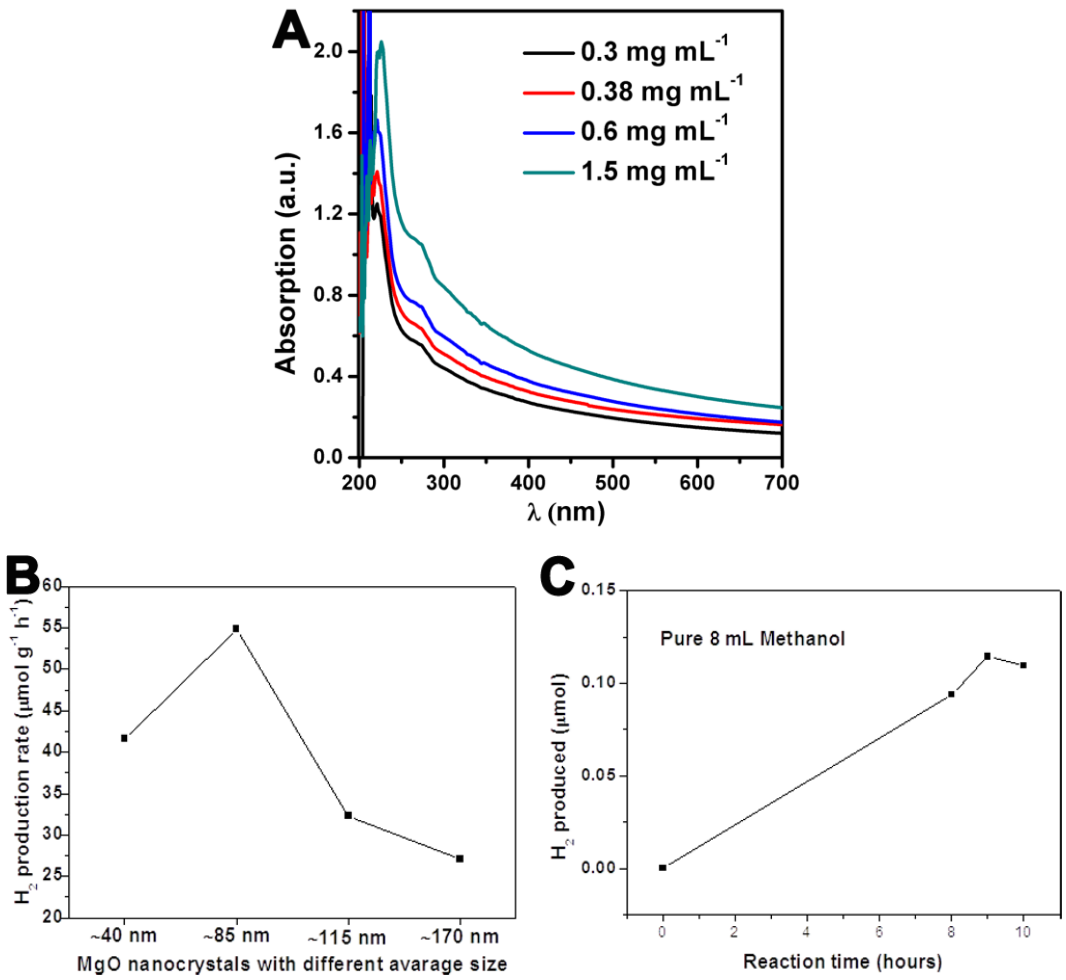

fig. S6. Optical properties for ~85 nm MgO nanocrystals and H_2 production from methanol photodecomposition. (A) Room temperature UV–vis absorption spectra of plasma-treated 85 nm sized MgO NPs in methanol with different concentrations. (B) H_2 production rate from MgO nanocrystals with different sizes (MgO concentration in methanol: 0.38 mg mL^{-1}). (**C**) H_2 produced from pure methanol without MgO under the same illumination conditions as used for the measurements in Fig. 4C.

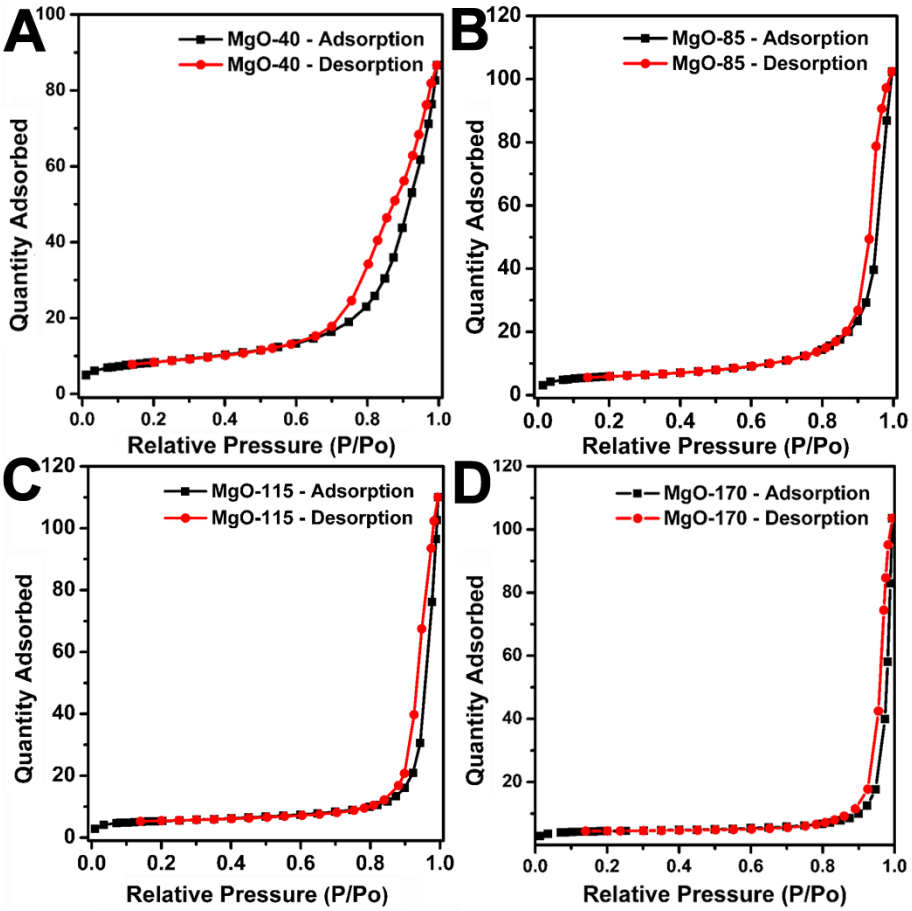

fig. S7. Specific surface area of four different-sized MgO NPs. Nitrogen adsorption and desorption isotherms measured at 77 K for MgO NPs with four different sizes, *i.e.* (**A**) ~40 nm, (**B**) ~85 nm, (**C**) ~115 nm and (**D**) ~170 nm, based on which the specific surface area is calculated by using the Brunauer-Emmett-Teller (BET) method.

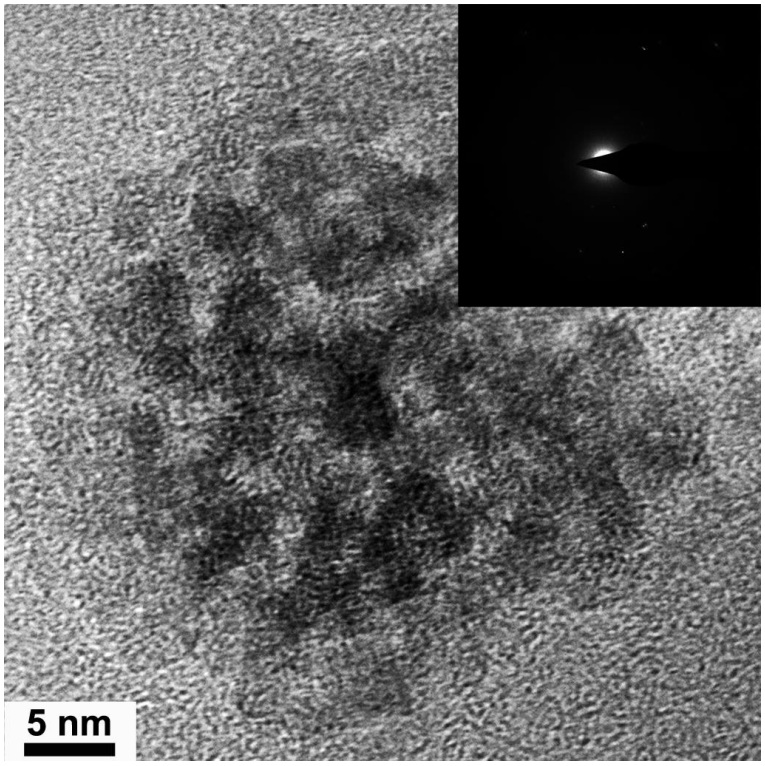

fig. S8. TEM and SAED images of an MgO NP with a size of 40 nm. TEM image of a single porous MgO nanoparticle with size of 40 nm, and the inset is the corresponding SAED image. As seen from SAED image, the ~40 nm sized MgO has low crystallinity degree.

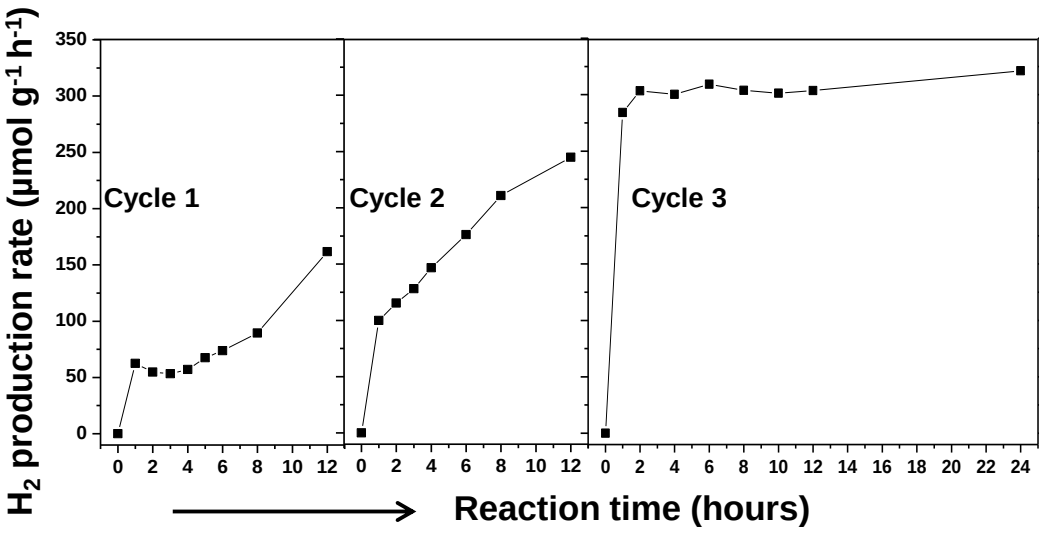

fig. S9. The rate pattern of H_2 production for ~85-nm MgO nanocrystals. H_2 production rate pattern for ~85-nm MgO nanocrystals based on the H_2 production results as presented in Fig. 4C.

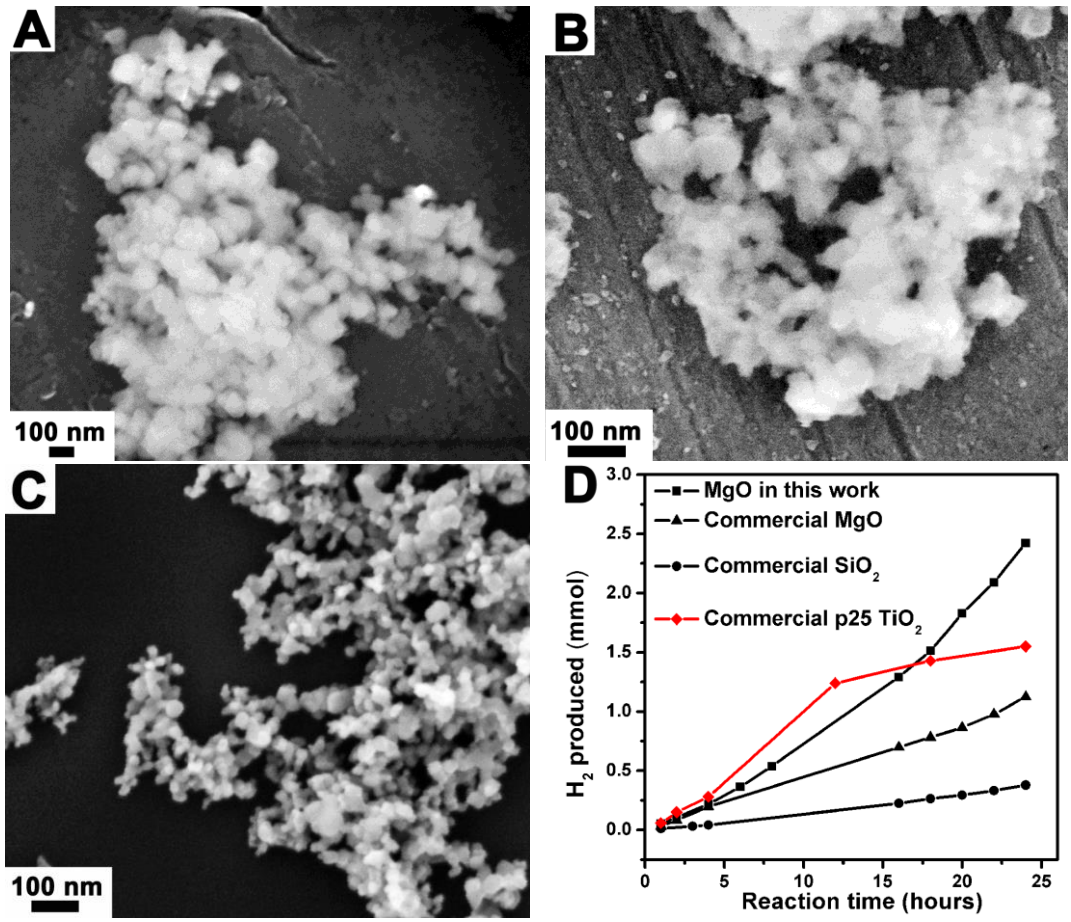

fig. S10. SEM analysis and H_2 production of commercial MgO, SiO_2, and TiO_2 (P25). The SEM images of commercial (A) MgO, (B) SiO_2, and (C) TiO_2 nanoparticles. (D) Comparison of H_2 production between MgO in this work, commercial MgO, commercial SiO_2 and commercial TiO_2 under the light illumination intensity of ca. 176 mW cm^{-2}.

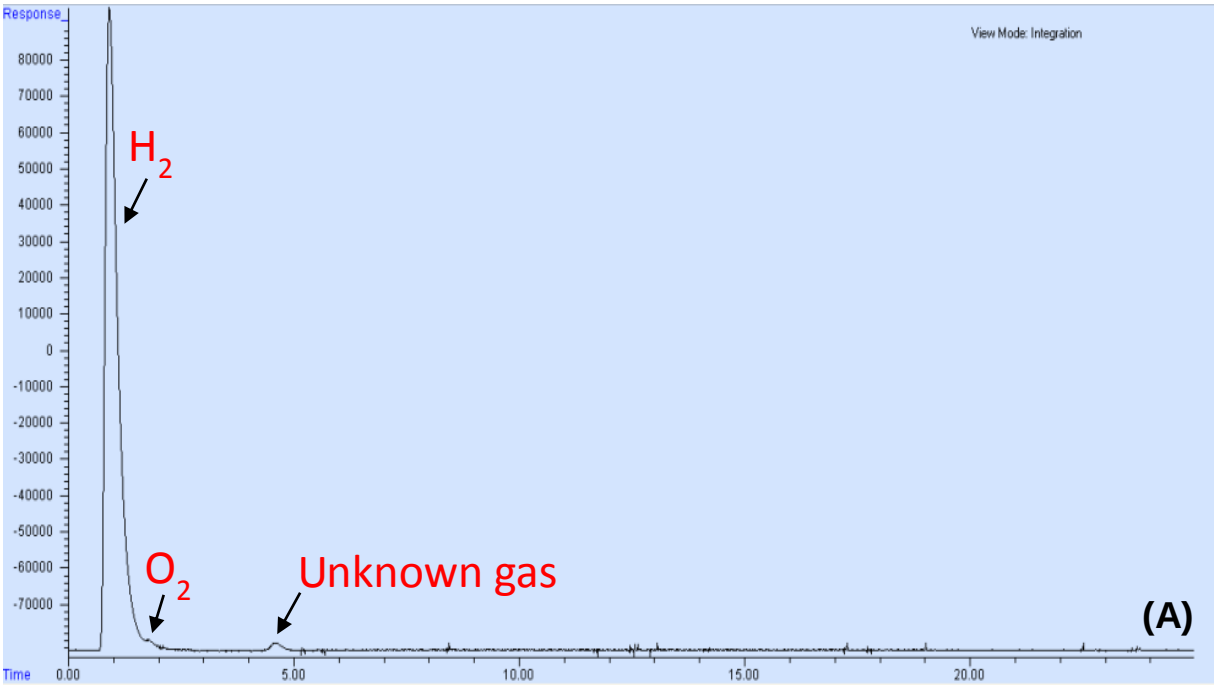
Response_
View Mode: Integration
80000
70000
60000
50000
40000
30000
20000
10000
0
-10000
-20000
-30000
-40000
-50000
-60000
-70000
H2
O2
Unknown gas
(A)
Time
0.00
5.00
10.00
15.00
20.00

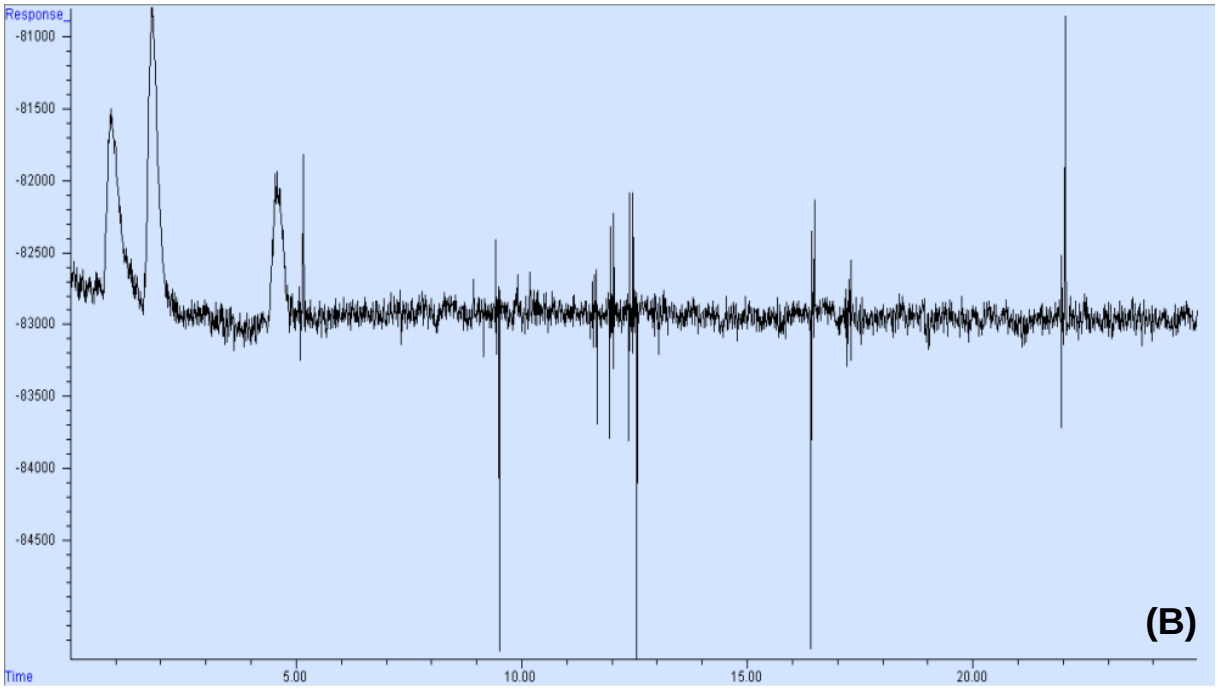
Response_
-81000
-81500
-82000
-82500
-83000
-83500
-84000
-84500
(B)
Time
5.00
10.00
15.00
20.00

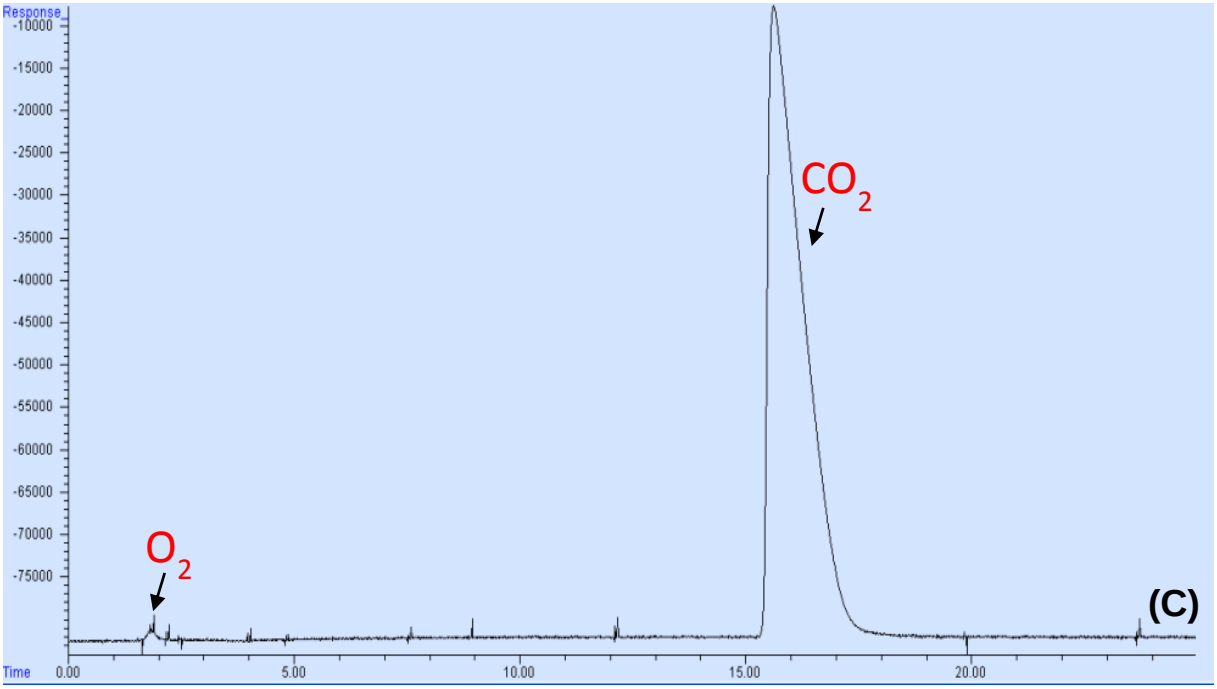

fig. S11. Chromatogram analysis of a mixture of gases. (**A**) 3mg MgO in 8 mL methanol after 48-hour photocatalytic reaction with 25-minute retention time in X-axis of chromatogram, (**B**) pure 8 mL methanol after 10-hour reaction, and (**C**) standard carbon dioxide (CO_2) gas.

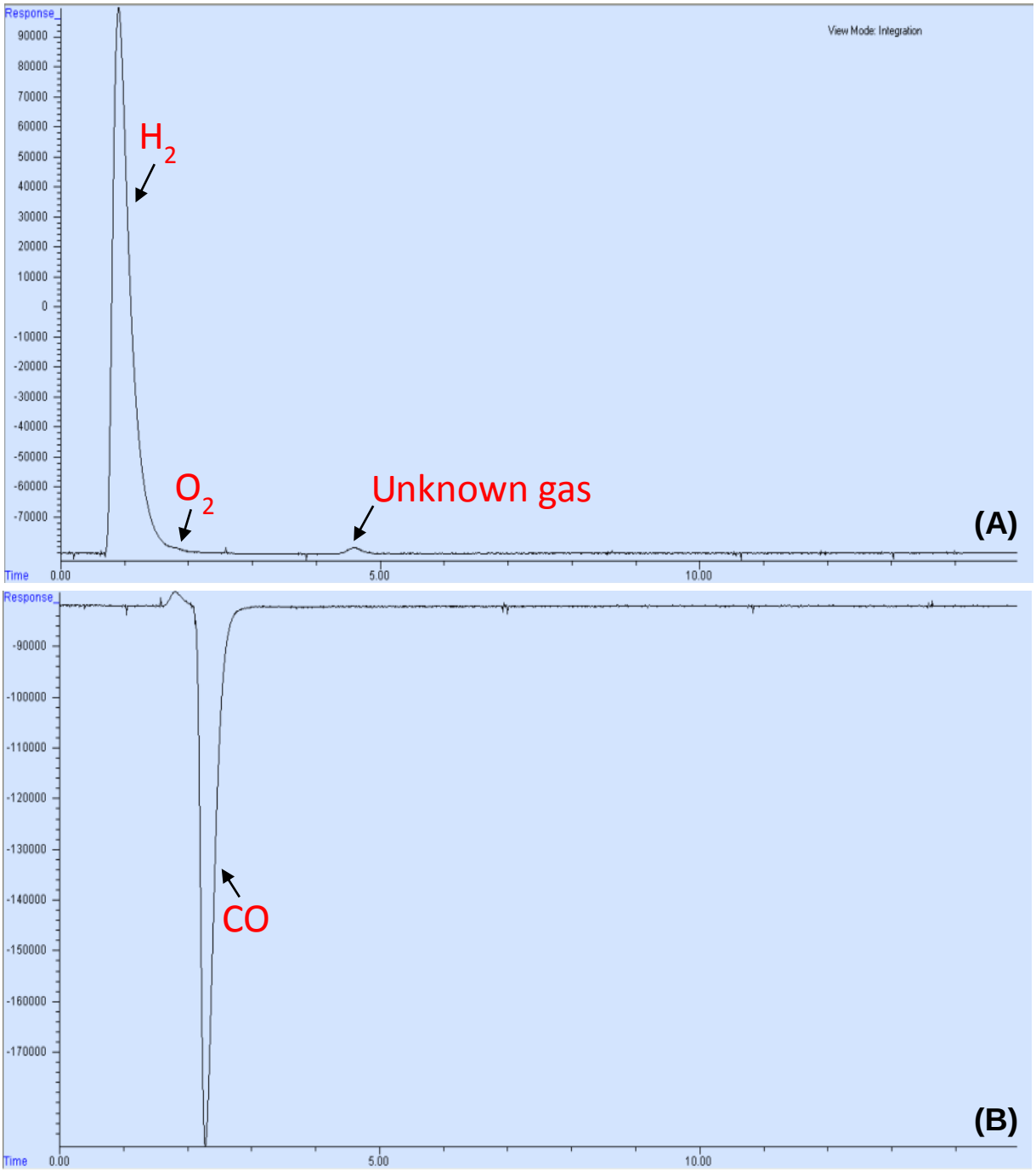

fig. S12. Chromatogram analysis of a mixture of gases. (**A**) 3mg MgO in 8 mL methanol after 48-hour photocatalytic reaction with 15-minute retention time in X-axis of chromatogram, and (**B**) the standard carbon monoxide (CO) gas.

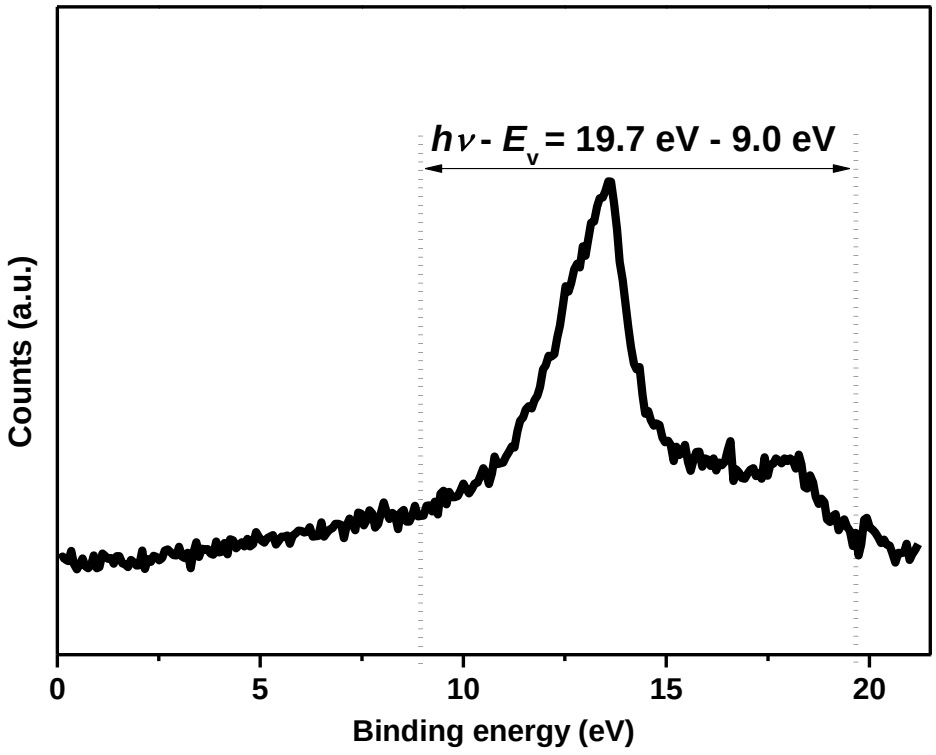

fig. S13. UPS spectrum for ~85-nm sized MgO NPs. UPS spectrum for ~85-nm sized MgO NPs based film (thickness ≈ 0.3 mm) taken with - 8 V bias applied to the sample.